2nd Advanced Optical Metrology Compendium

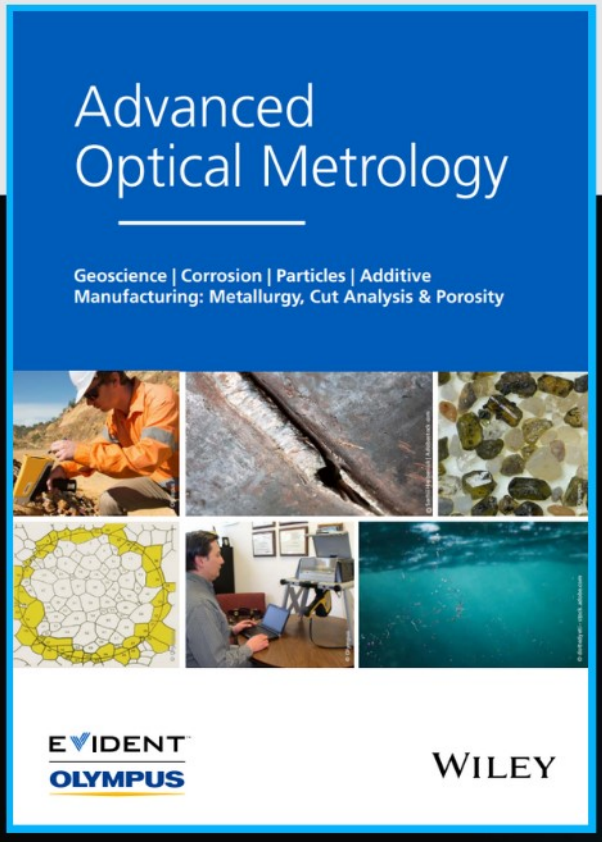

The latest eBook from Advanced Optical Metrology. Download for free.

This compendium includes a collection of optical metrology papers, a repository of teaching materials, and instructions on how to publish scientific achievements.

With the aim of improving communication between fundamental research and industrial applications in the field of optical metrology we have collected and organized existing information and made it more accessible and useful for researchers and practitioners.

EVIDENT
OLYMPUS

WILEY

NANO · MICRO small
www.small-journal.com

4D Direct Laser Writing of Submerged Structural Colors at the Microscale

Bingrui Liu, Bin Dong, Chen Xin, Chao Chen, Leran Zhang, Dawei Wang, Yanlei Hu, Jiawen Li, Li Zhang, Dong Wu, and Jiaru Chu*

Biomimetic stimuli-responsive structure colors (SCs) can improve the visualization and identification in the micro functional structure field such as information encryption/decryption and smart actuators. However, it is still challenging to develop the ability to 4D print arbitrary submerged colorful patterns with stimuli-responsive materials at the microscale. Herein, a hydrogel photoresist with feature resolution (98 nm) for the fabrication of 4D microscopic SCs by the femtosecond direct laser writing method is developed. The 4D printed woodpile SCs are grouped as pixel palettes with various laser parameters and they spanned almost the entire color space. The coloring mechanism of diffraction gratings is not only investigated by optics microscopy and spectroscopy but also supported by simulation. Moreover, the 4D printed hydrogel-integrated amphichromatic fish constructions and pixelated painting can visually discolor reversibly by regulating the solution pH. This finding promises an ideal coloring method for sensors, anti-counterfeiting labels, and transformable photonic devices.

1. Introduction

In recent years, with the rapid development of micro functional structure fields such as information encryption/decryption[1,2] and smart actuators,[3] there is an increasing demand for various stimuli-responsive structure colors (SCs) to improve the visualization and identification in different conditions.[4–7] However, some existing stimuli-responsive SCs can only achieve switching of structure and optical properties in air conditions, and can't achieve responsive SC changes under complex solutions.[8–10] Inspired by the underwater color and texture variations of cuttlefish,[11] various stimuli-responsive materials (SRM) with biomimetic submerged SCs including liquid crystalline elastomers,[12] cholesteric liquid crystals[13] and hydrogel[14,15] have been developed. Among them, owing to the good biocompatibility, tunable toughness, high water content and reversible volume change, pH-responsive hydrogel (PRH) has been extensively studied that enables the sensing or display application through the transformation of shape in the solution.[16,17] For instance, Zhu et al. developed a pH-responsive device by coating acrylic acid (AAC) and acrylamide (AAm) via in situ copolymerization onto *Papilio Paris* wings having lamellar structure, which provided the photonic crystals (PCs)-based pH sensor.[18] In addition, Park et al. presented a 3D display based on multi-order reflection SCs with P2VP hydrogel. This display exhibits distinct reflective colors upon pH-induced swelling and deswelling of P2VP (pKa ≈ 4).[19] Nevertheless, these methods for preparing macroscopic SCs either require immobilized templates or complex post-processing methods, which can't be applied to microscopic polychromatic SCs. Importantly, the morphing of these PRH structures was only achieved at pH ≈4 or ≈9, which is not suitable for a neutral pH biomedical application (pH ≈ 7.4).[19,20] Therefore, it remains challenging to develop a new technique to print arbitrary SCs with a novel pH-responsive hydrogel at the microscopic scale.

Fortunately, the femtosecond direct laser writing (fs-DLW) technique via two-photon polymerization (TPP) has been demonstrated as an emerging method for manufacturing arbitrary structures with a sub-micron lateral resolution,[21–24] thus enabling the fabrication of 4D photonic structures with stimuli-responsive materials.[25] fs-DLW has obvious advantages of true 3D programmable ability and submicron printing resolution, representing a more effective strategy to construct complex functional microarchitectures.[26,27] In addition, 4D printing of microscopic SCs by employing fs-DLW has already been adopted for the construction of humidity-sensitive micro-actuators[28] and shape-memory grid structures,[29] in addition to magnetism-switching photonic crystals.[30] Although these reported SCs exhibited a controllable change in terms of polychromatic or morphology under air conditions, they are not sufficient for the identification and tracking of microrobots or actuators in solution conditions. Recently, 4D micro-printing of high-resolution, polychromatic, and

B. Liu, B. Dong, L. Zhang, D. Wang, Y. Hu, J. Li, D. Wu, J. Chu
CAS Key Laboratory of Mechanical Behavior and Design of Materials
Department of Precision Machinery and Precision Instrumentation
University of Science and Technology of China
Hefei, Anhui 230027, P. R. China
E-mail: dongwu@ustc.edu.cn
C. Xin, L. Zhang
Department of Mechanical and Automation Engineering
The Chinese University of Hong Kong
Shatin NT, Hong Kong 999077, P. R. China
C. Chen
School of Materials Science and Engineering
Hefei University of Technology
Hefei 230009, P. R. China
The ORCID identification number(s) for the author(s) of this article can be found under https://doi.org/10.1002/smll.202204630.

DOI: 10.1002/smll.202204630

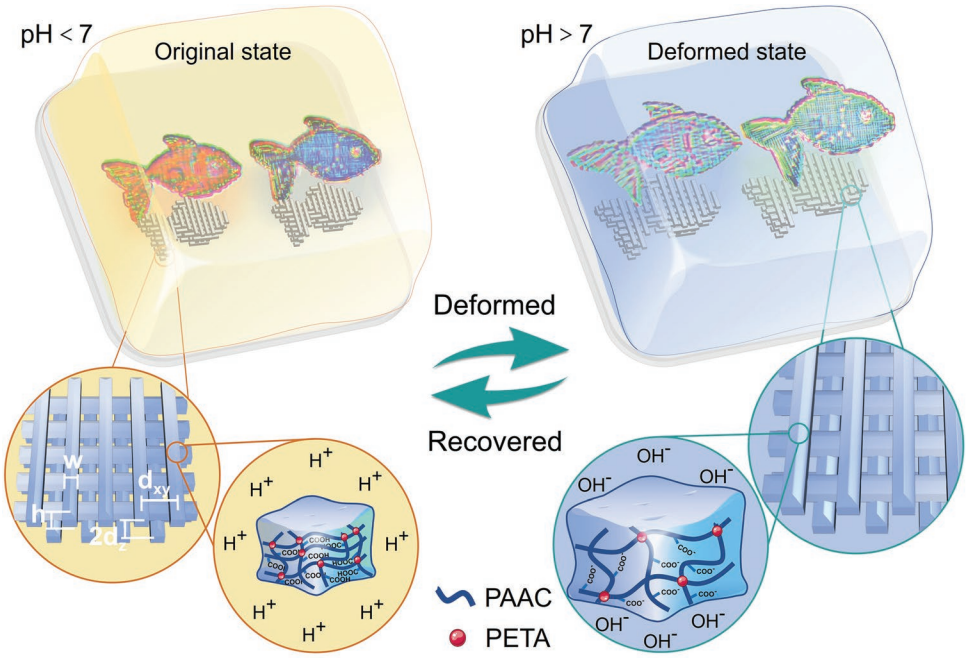

Figure 1. Schematic illustration of the color and shape changes of 4D printed microstructures using a pH-responsive hydrogel (PRH). The printed woodpile structures show a significant structural color in pH < 7 solutions. The deformation of the structures at pH > 7 solutions render it color changed, where it remains in a reversible color after changing the pH of the solution back. The electrostatic repulsion forces between carboxylate ions in acrylic acid (AAC) repel other molecular chains, resulting in a significant expansion of the polymer grid in the basic solution.

morphology-controllable submerged PRH-based SC devices by using fs-DLW is scarcely involved but highly desirable.

Herein, we develop a new solvent-free hydrogel recipe that allows 4D printing of programmable microscopic photonic structures by the fs-DLW techniques, utilizing a modified pH-sensitive hydrogel with a resolution of 100 ± 2 nm. Thanks to its rapid responsivity to solution pH within 480 ms, the hydrogel-constructed SC device could be reversibly switched between the swelling and deswelling operation in a more biocompatible environment (pH ≈ 7) than previously reported (**Figure 1**). Additionally, we have systematically investigated the influence of layer numbers, writing speed, laser power, rod width, height, and interval on the SC displays. On this basis, the presentation of the SC device could be readily designed to cover almost the entire red–green–blue (RGB) color space in the CIE 1931 chromaticity diagram. Moreover, fundamental optics microscopy/spectroscopy and finite-difference time-domain (FDTD) grant us a deeper understanding of the underlying mechanism of color-switching of SC devices. Last but not least, by regulating the solution pH, the hydrogel-integrated amphichromatic fish and pixelated paintings could visually discolor in a reversible manner. The current approach to pH-responsive microscopic SC device is convinced to be profound guidance for the researchers occupied in identifiable and traceable features in the microscopic domain.

2. Results and Discussions

2.1. TPP Lithography of the pH-Responsive Biocompatible Hydrogel

Different from the reported use of a solvent to dissolve the solid thickener polyvinylpyrrolidone (PVP),[31] the hydrogen bond between PVP and AAC was used to directly dissolve the PVP by ultrasonic method without any other solvents (**Figure 2**a, S1, Supporting Information), which can increase the photoreactive group densities and the viscosity. As shown in Figure S2, Supporting Information, our prepared precursor is homogeneous and transparent without any solid particles. It is worth mentioning that all components in the formulation were entirely commercially available to provide maximum accessibility and avoid additional chemical modification. Compared with solvent-based hydrogel precursors (Figures S3 and S4, Supporting Information), we can see a better resolution with our new solvent-free PRH under the same printing script. Although only present in small concentrations, the photoinitiators can excite free radicals through two-photon absorption, which caused the polymerization of monomers and crosslink. We developed three hydrogel photoresists with different photoinitiators 4,4′-bis(diethylamino) benzophenone (EMK), diphenyl(2,4,6-trimethylbenzoyl) phosphine oxide (TPO), and 7-diethylamino-3-thenoylcoumarin (DETC). The scanning electron microscope (SEM) images show the free-hanging lines produced between two blocks become thinner and thinner as the direct writing speed increases from 200 to 500 μm s^{-1}. The thinnest free-hanging wire was 96 ± 5 nm for the precursor using EMK, 102 ± 9 nm for the precursor using TPO, and 125± 6 nm for the precursor using DETC (Figure S5a, Supporting Information). But the ridges at the turning points in the pyramids are considerably larger when TPO is the photoinitiator than when EMK is used.[32] So, the EMK was chosen as the ideal photoinitiator to ensure the fs-DLW structure with excellent structural integrity (Figure S5b, Supporting Information). To explore the minimum print resolution of our hydrogel materials, printing 2D line grating is a common method.[29,33] As shown in Figure S6,

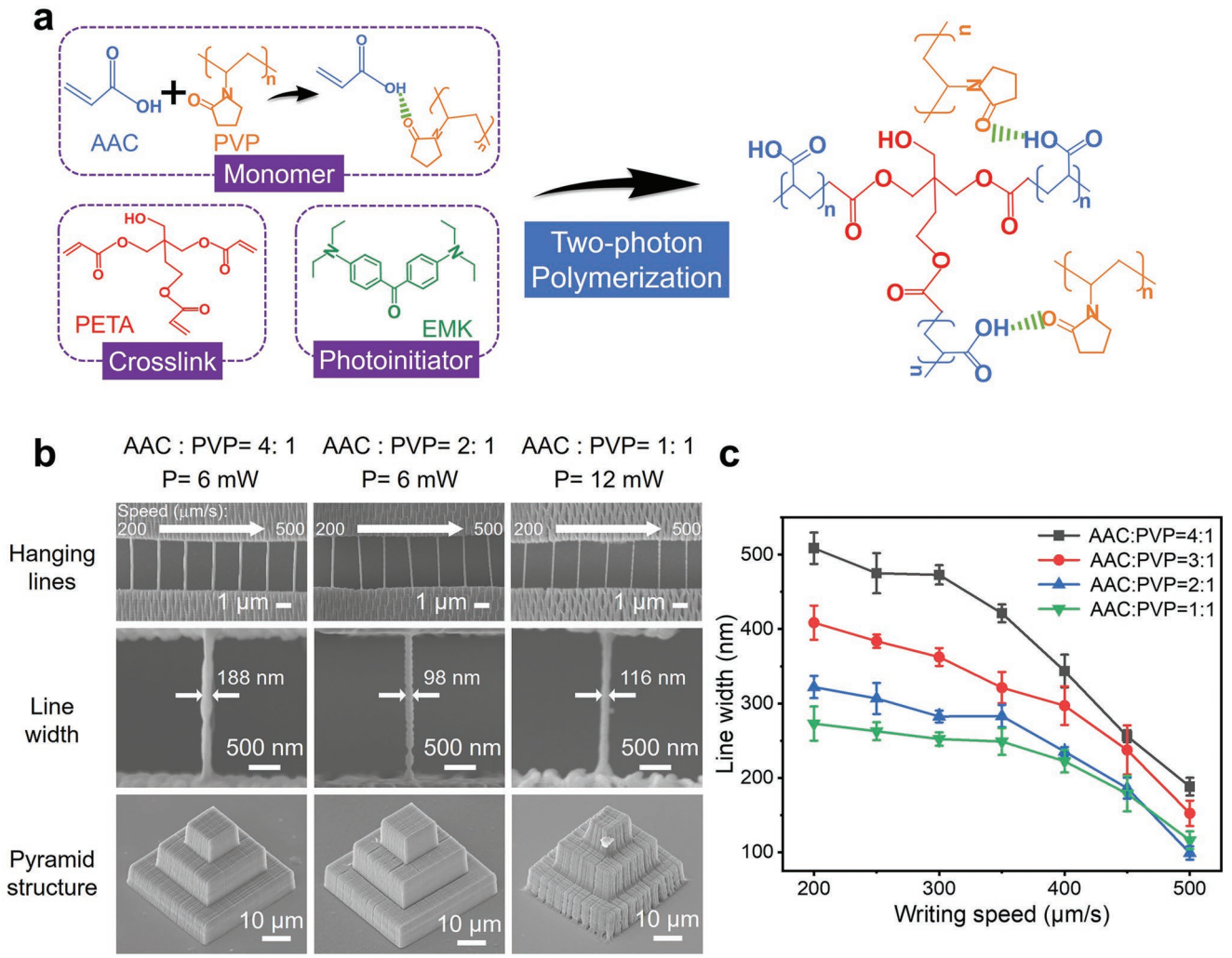

Figure 2. Schematic of the TPP process. a) The PRH includes AAC and PVP as the monomer, PETA as the crosslink, and EMK as the photoinitiator. b) Free-hanging lines were produced between two blocks and pyramids using the PRH with different ratios of AAC:PVP. The laser power was adjusted according to the integrity of the free-hanging lines. c) The curves about the line width change with the writing speed for PRH with different ratios of AAC:PVP. All data were averaged using 3 measurements of individuals and the error bars were calculated as the standard deviation from the mean.

Supporting Information, the minimum linewidth is 175 nm (Figure S6, Supporting Information), which is larger than the suspended line but is also better than that of other stimuli-responsive hydrogel material.[34]

Then we also discuss the resolution and structural integrity of PRH with different ratios of AAC to PVP. For all precursors, the free-hanging lines produced between two blocks become thinner and thinner as the writing speed increases from 200 to 500 μm s^{-1}. When the amount of PVP added is very small, such as the weight ratio of AAC:PVP is 4:1, the width of the free-hanging line is stronger, but the structural integrity is very good (Figure 2b). When the ratio of AAC:PVP is reduced to 2:1, the width of the free-hanging line is reduced to 100 ± 2 nm. As the weight of PVP in the formulation was further increased, the laser power required to maintain structural integrity was higher. When the ratio of AAC:PVP is 1:1, the width of the free-hanging line is 116 ± 12 nm, which is not much different from the ratio of 2:1 (Figure 2c). Nevertheless, the two-photon polymerization (TPP) of AAC:PVP = 1:1 hydrogel photoresist can't be triggered at 6 mW power. The surface of the pyramid structure prepared by the ratio of AAC:PVP = 1:1 is not complete. So, the high resolution obtained is very relevant for the free radical polymerization process, the PRH with AAC:PVP = 2:1 is the ideal suitable formulation to ensure an excellent structural integrity of fs-DLW structures.

The printed structure by our PRH exhibited excellent pH-responsive properties because the pendant acidic (carboxylic) groups exhibited weak and strong electrostatic repulsions in acid and alkaline solutions, respectively (Figure 1). In order to quantify the realistic deformation range of the pH-responsive structure during the expanded–contracted state, the expansion ratio (ε_e and ε_c) is defined as the ratio of the length difference between the expansion state or contracted state to the contracted length, as shown in Figure S7, Supporting Information.[25] Therefore, the expansion ratio can reflect the relative deformation capacity of the structures. As shown in Figures S8–S10, Supporting Information, the typical relative expansion ratio (RER) of both cubic plate and single rod of the

PRH was measured to be 45%. From the SEM images of the suspended line in the alkali condition (Figure S11, Supporting Information), we can see that the expansion rate of the single suspended line is 42.9% in the swelling environment, which is similar to the result we observed with an optical microscope. The SEM images and experimental observation also reveal that this PRH has good homogeneity and isotropic swelling characteristics once the solution pH is greater than 7 (Figure S9a, Supporting Information), which has more advantages in terms of biocompatibility. According to the analysis of the Cell Counting Kit-8 (CCK-8) test, the total cell viability with our PRH at different time points was all higher than 96%, which was not significantly different from the control (Figure S12, Supporting Information). To evaluate the fatigue resistance of the printed PRH, the expansion ratio of the cubic plate is measured with multiple expansion and contraction cycles (Figure S9b, Supporting Information), validating the good repetition performance of the PRH. By changing the laser processing parameters, the expansion ratio can be quantitatively regulated. As shown in Figure S13, Supporting Information, not only is the response speed of the cubic structure by the new PRH we developed reduced down to a sub-second level (480 ms), but also the response speed of the complex woodpile structure can be maintained in the sub-second level (850 ms).

2.2. Polychromatic Structure Colors

Different 2D microstructures have been reported for printing responsive photonic crystals in the air,[35] The 3D woodpile structure was chosen because of its simple construction, rapid patterning, and high mechanical stability.[33,36] After summarizing the prior art regarding DLW of color responsive components in Table S1, Supporting Information, our work has a high resolution of DLW using the acrylic-based hydrogel-based photoresists, the minimum feature size of the previously reported DLW crosslinked acrylic copolymer was 500 nm. Our work also enables the fabrication of arbitrary 3D polychromatic structures using a single material, with pH-dependent color modulation under submicrometer size. As shown in **Figure 3**a, the woodpile structure consists of orthogonal grating stacks, where d_{xy} and d_z represent the lateral and axial constants of the woodpile structure, w and h represent the width and height of the constituent rods. This polymeric woodpile structure (Figure 3b) with various d_{xy} and d_z parameters was directly written by using a femtosecond laser two-photon lithography system and formulated PRH. We investigate the different colors achieved by the blocks with the woodpile structure and how these colors depend on the various designed parameters. A series of transmittance optical micrographs of the color palette was obtained at a range of laser power (6, 8, and 14 mW). From the SEM image of the woodpile structure observed from the side view (three different SCs within the black box are plotted in Figure 3e), it can be seen that the rod width and rod height of the woodpile increase with the printing laser power, but the aspect ratio remained almost unchanged (Figure 3c,d). The two parameters d_{xy} and d_z can be varied by using MATLAB to create different 3D models. To study the effect of d_{xy} and d_z on color, we fabricated structures with a constant writing speed of 300 μm s^{-1}. When d_z is smaller than 0.8 μm, the adjacent lines merge during the polymerization process, resulting in a series of nearly transparent patches at different d_{xy}. When d_z is bigger than 1.2 μm, the gap between two layers is too large, causing only yellow and blue to display with the variation of d_{xy}. Thus, $d_z = 1.0$ μm was chosen for our following study. The SEM images (Figure S14, Supporting Information) of the top and side view show detailed woodpile structures with d_{xy} ranging from 0.7 to 1.2 μm. A detailed feature size of 308 nm width of the rod has shown in Figure S15, Supporting Information, which further demonstrates that this size is more suitable for 2D grating models. We map the color coordinates of Figure 3e to the CIE 1931 chromaticity diagram, demonstrating a fairly wide range of colors (Figure 3f), spanning almost the entire red–green–blue (RGB) color space. Itten's Color Wheel consists of three primary colors (red, yellow, and blue), three secondary colors (orange, green, and purple), and six tertiary colors; and twelve printed color pixels with corresponding colors encircled the wheel (Figure S16, Supporting Information). Also, as shown in Figure S17, Supporting Information, the structural color also changes with the change of the horizontal angle. When the horizontal angle reaches about 15°, the diffraction color changes significantly.

2.3. Coloration Mechanism of SCs

To better understand the color generation of this design, we measured the transmission spectrum of the woodpile structure and performed FDTD simulations to obtain the spectrum (**Figure 4**a). As shown in Figures S18 and S19, Supporting Information, the refractive index n and extinction coefficient k of the PRH at both swelling or deswelling states were fitted based on the measured Δ and Ψ using the Cauchy dispersion function.[29,37] The simulation results show a good qualitative agreement with the experiment. A red-shift effect of the spectral position is observed in Figure 4a. Since the increase in the number of layers only improves the purity and contrast of the SC, there is no color change with the increase in the number of layers (Figure S20, Supporting Information). When a beam of polychromatic light is incident on the woodpile structure, the transmitted beams are diffracted by the different layer. As shown in Table S2, Supporting Information, diffraction orders and corresponding colors of gratings are calculated by Equation (S9), Supporting Information, with different structural parameters. The simulated near-field electric field phase and amplitude for one periodic woodpile structure (fabricated with the laser power of 8 mW, write speed of 300 μm s^{-1}, and the d_z of 1.0 μm) at the wavelength of 430 and 600 nm are shown in Figure 4b and Figure S21, Supporting Information, respectively. The wavelength of 430 and 600 nm corresponds to the marked peak and dip of the spectrum in Figure 4a. The incident plane waves are assumed to pass through the glass substrate without scattering. After propagating through the woodpile structure, the wavefront is delayed compared to the wave fronts that pass through the water gap. As shown in the near-field phase plot in Figure 4b, the regions inside and directly above the rod line appear to accumulate phase faster than the middle region. The interference of these two transmitted light regions results in some focusing and redistribution of the optical energy flow (see the corresponding near-field electric field amplitude in Figure S21, Supporting Information), which results in strong coupling between orthogonally polarized waves at

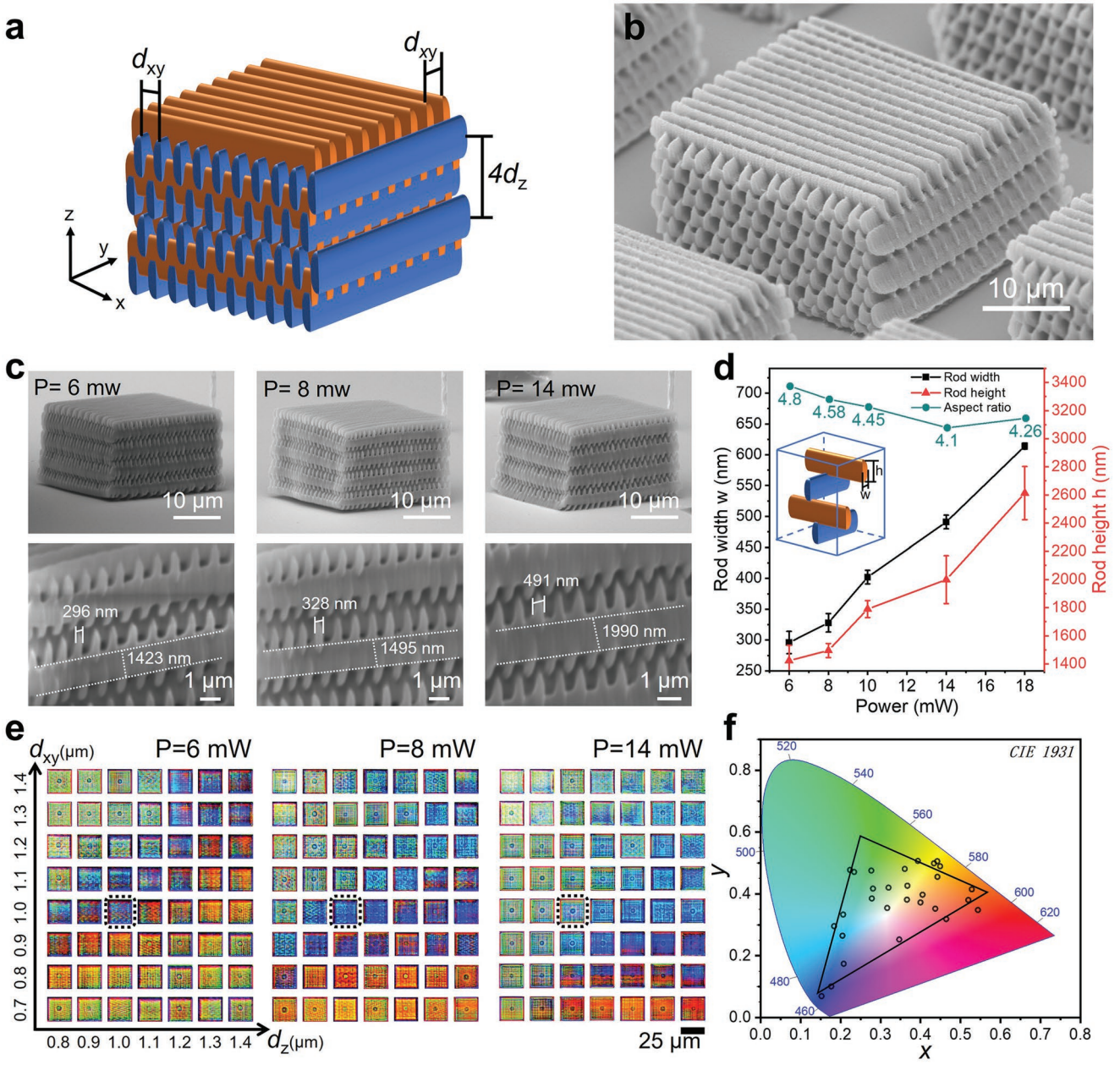

Figure 3. Polychromatic structure colors underwater and scanning electron micrographs (SEM) of woodpile structures. a) Schematics illustration of the woodpile structure. b) The SEM image of the woodpile structure. c) SEM image of the variation of rod width and height with different laser power, keeping the d_z = 1.0 μm and d_{xy} = 1.0 μm. d) Variation curves of rod width and height under different laser powers. The data of rod width and height were averaged using 3 measurements of individuals and the error bars were calculated as the standard deviation from the mean. e) Optical transmittance micrographs of printed color palette for a constant pitch of 25 μm but different d_{xy} and d_z at a range of laser power (6, 8, and 14 mW, respectively). Optically characterized NA is 0.65. f) The calculated color coordinates of Figure 3c are mapped onto the CIE 1931 chromaticity diagram, indicating the color gamut achieved from the woodpile structures.

the wavelength of 430 nm. For the peak and dip positions, constructive interferences occur at different parts above the structure. The far-field energy distribution can be obtained by performing the near-field to far-field transformation. Figure 4c shows the normalized far-field electric field amplitude within the objective collection angle (CA) for the dip (600 nm) and peak position (430 nm), respectively, corresponding to the experimental observations of the objective lens adopted in our experiment (the CA = 23.6°). The integration of the far-field electric intensity within the CS results in the transmittance spectra dip and peak shown in Figure 4a.

Woodpiles with different constants can be freely positioned and concatenated into a single object to enable color printing of 3D structures. To demonstrate the ability to print arbitrary and complex 3D color objects at the microscopic level, we fabricated microscopic models of fish (Figure 4d) and owl (Figure S22, Supporting Information) composed of woodpile structures. The fs-DLW format layout was generated by using MATLAB to create a 3D model of

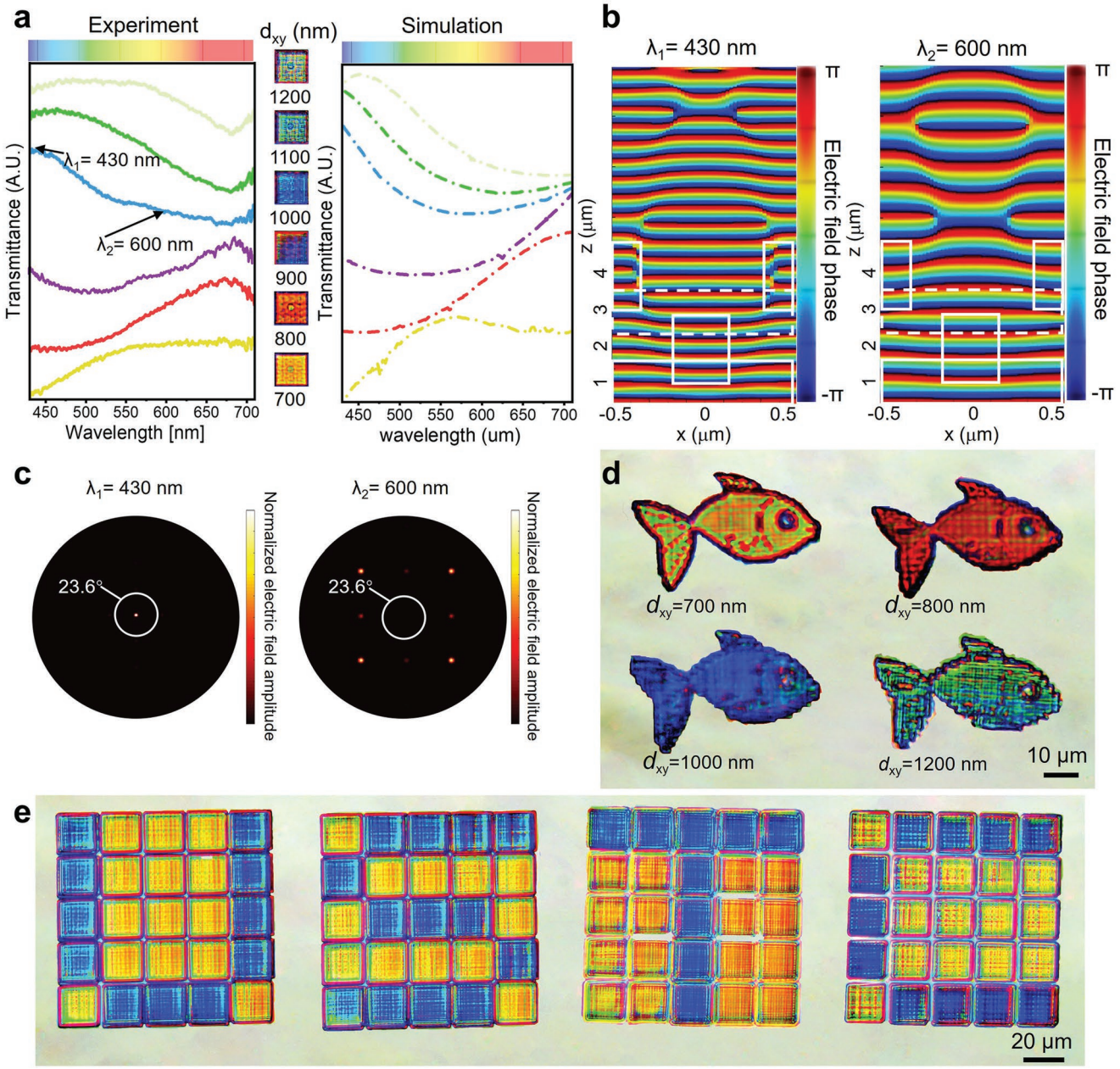

Figure 4. Finite difference time domain (FDTD) analysis of the SCs. a) Measured and FDTD simulated transmittance spectra of structures with different d_{xy} (from the black dashed rectangle in Figure 3c ranging from 0.7 to 1.2 μm). Marked positions $\lambda_1 = 430$ nm and $\lambda_2 = 600$ nm are used for FDTD field analysis in Figure 4b,c and Figure S16, Supporting Information. b) Cross-section view of nearfield normalized electric field phase and amplitude for a cycle of woodpile structure (laser power: 8 mW, write speed: 300 μm s^{-1}, $d_{xy} = 1.0$ μm, $d_z = 1.0$ μm) at dip transmittance 600 nm and peak transmittance 430 nm wavelength, respectively. The white box area represents one periodic woodpile structure. c) Top view of far-field normalized electric field amplitude for the above grid structure at dip transmittance 600 nm and peak transmittance 430 nm wavelength, respectively; the white circle represents the collection field for the microscope used in this work (CA = 23.6°). d) The fish structure with the woodpile. e) Optical transmittance micrographs of two printed color palettes for a constant pixel of 25 μm but varying d_{xy} and d_z for a range of laser power.

fish with different d_{xy} of the woodpile structures. The optical micrographs in Figure 4d, and Figures S15 and S23, Supporting Information, show that the woodpile fish have a robust shape and structure, exhibiting polychromatic colors. Furthermore, we successfully fabricated the pixelated structures with two different constants of d_{xy} = 0.7 (yellow) and 1.0 μm (blue) under a fixed $d_z = 1.0$ μm and scanning speed of 300 μm s^{-1}. The letters U, S, T, and C are represented in Figure 4e, which demonstrates a simple application using the fs-DLW technique with our PRH. The image of each letter consists of 5 × 5 pixels, and each pixel is designed to be 20 μm.

2.4. pH-Triggered Switching of SCs

The pendant carboxylic groups exhibited weak and strong electrostatic repulsions in acid and basic solutions,

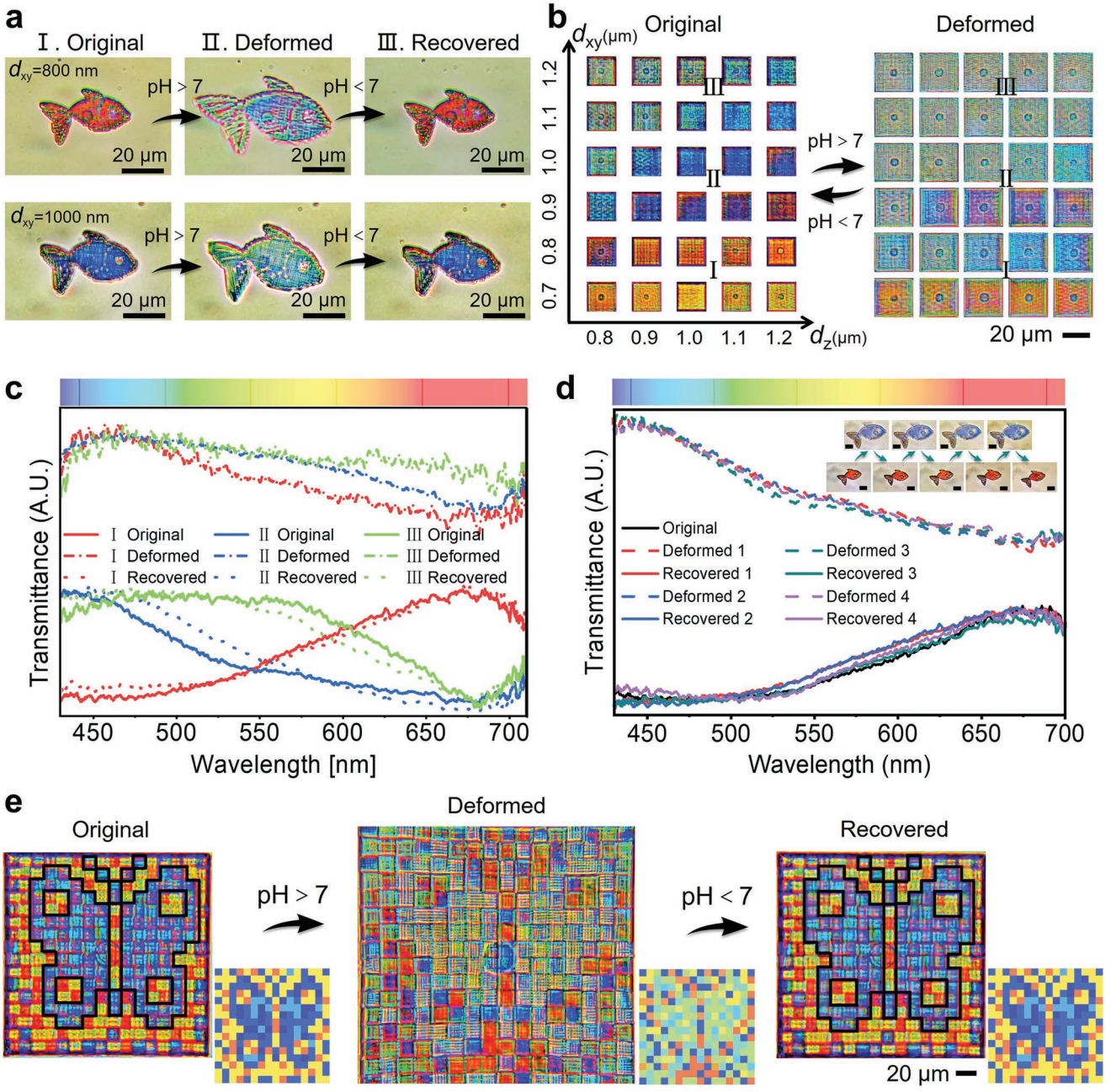

Figure 5. pH responsive structure and colors change. a) Measured optical micrographs show the color change of red and blue woodpile fish in original, deformed, and recover status, respectively. In order to avoid the limitation of the substrate on the structure's expansion and contraction and to fix the structure on the substrate, the different structures were fabricated on elongated cylindrical bases with 10 μm high. b) Different colors in original or deformed status were observed by the objective lens (CA = 23.6°) in transmittance mode (the laser power was kept at 8 mW, and the d_z was varying from 0.8 to 1.2 μm with a step of 0.1 μm in the transverse direction, and the d_{xy} was varying from 0.7 to 1.2 μm with a step of 0.1 μm in the vertical direction). The support micropillars with a semidiameter of 4 μm are added to prevent the structures in (a) and (b). c) Comparison of measured spectra in original and deformed status for three different grid structures (marked as I, II, and III in Figure 5b). d) Measured spectra of four swelling-deswelling cycles of red woodpile fish. Scale bars represent 10 μm. e) The butterfly painting deforms as the pH of the solution change. The support micropillars with a semidiameter of 10 μm are added to prevent the structures detached from the substructure.

respectively.[38] With the swelling or deswelling of the woodpile structure, the color of the fish and owl can also switch rapidly (**Figure 5**a, and Figure S22 and Movie S1, Supporting Information). As we before mentioned in Figures S10 and S11, Supporting Information, the PRH material we prepared has about 45% expansion ratio for simple block structures or suspended lines in alkaline conditions. To further investigate the pH-triggered swelling or deswelling of the submicron scale woodpile structure, we printed a color palette (Figure 5b) with a fixed laser power of 8 mW and a write

speed of 300 μm s^{-1} but varied the d_{xy} and d_z from 0.7 to 1.2 μm horizontally with a step of 0.1 and 0.8 to 1.2 μm vertically with a step of 0.1 μm, respectively. The solution was then changed to a weakly alkaline environment (pH > 7) with 0.1 M NaOH solution added drop by drop, the overall woodpile structure also expanded by about 45% and the palette color changed rapidly, respectively. When the environment was changed back to acidic by the dropwise addition of 0.1 M HCl solution, all colors were recovered (Figure 5b). Due to the complex woodpile structure and overall large volume, the recovery process occurs in ≈850 ms. We compared the spectra of three different colors (labeled I, II, and III in Figure 5b) before and after the swelling and recovery process, as shown in Figure 5c. The spectra of the original and recovered colors are nearly identical, indicating the good recoverability of our 4D printed hydrogel structures. The robustness of the woodpile fish structure was checked in Figure 5d by programming its swelling and deswelling four times, the spectra for recovered structures in different cycles match well, indicating good repeatability of the woodpile structure. To demonstrate potential applications, we printed artwork images with blue butterflies, just like the "hidden digit" method used for color-blindness testing (Figure 5e original and Movie S2, Supporting Information). The image consists of 16 × 16 pixels, each designed to be 8 × 8 $μm^2$, which shows a distinct butterfly in its original state. The painting was then swelled into a "hidden" image (Figure 5e deformed) by adding the basic solution. The blue butterfly disappeared because the color of the butterfly and its surroundings changed. The pH of the solution was adjusted to <7 by adding 0.1 M HCl solution, and the painting returned to the "display" state. A similar "hidden digit" approach can also be used to encrypt QR codes or DM codes as shown in Figure S24, Supporting Information. Herein, we demonstrate optical changes in pixel patterns triggered by solution pH, a simple application for visual identification using our new PRH-printed submerged SCs.

3. Conclusion

To sum up, a novel solvent-free PRH was successfully prepared. By controlling the geometry of the woodpile structure at the submicron level, a series of submerged SCs was achieved, spanning nearly the entire RGB color space in the chromaticity diagram. The simulated spectra were obtained using the diffraction grating mechanism by the FDTD, which was in good agreement with the experimental results. The color-switching behavior was successfully achieved through the expansion of the woodpile structure when the pH of the solution was greater than the ionization threshold. This approach will open up potential applications of 4D printing with PRH in the information encryption/decryption and anti-counterfeiting label fields.

Supporting Information

Supporting Information is available from the Wiley Online Library or from the author.

Acknowledgements

This work was supported by the National Natural Science Foundation of China (Nos. 52005475, 61927814, 52122511, 91963127, 52075516), the Major Scientific and Technological Projects in Anhui Province (201903a05020005), the Fundamental Research Funds for the Central Universities (WK2090050048, WK5290000003), the Open Project Program of Wuhan National Laboratory for Optoelectronics (No. 2019WNL0KF014), and the Open Research Fund of Advanced Laser Technology Laboratory of Anhui Province (No. AHL2020KF01). This work was also partially supported by the Hong Kong Research Grants Council (RGC) under Project No. JLFS/E-402/18. The authors acknowledge the Experimental Center of Engineering and Material Sciences at USTC for the fabrication and measurement of samples. This work was partially conducted at Key Laboratory of Aero Engine Extreme Manufacturing Technology of Zhejiang Province. This work was partly carried out at the USTC Center for Micro and Nanoscale Research and Fabrication.

Conflict of Interest

The authors declare no conflict of interest.

Data Availability Statement

The data that support the findings of this study are available from the corresponding author upon reasonable request.

Keywords

direct laser writing, femtosecond lasers, four-dimensional printing, pH-responsive hydrogels, structure colors

Received: July 28, 2022
Revised: October 6, 2022
Published online:

[1] W. Hong, Z. Yuan, X. Chen, *Small* **2020**, *16*, e1907626.
[2] H. Shi, S. Wu, M. Si, S. Wei, G. Lin, H. Liu, W. Xie, W. Lu, T. Chen, *Adv. Mater.* **2022**, *34*, 2107452.
[3] X. Li, J. Liu, D. Li, S. Huang, K. Huang, X. Zhang, *Adv. Sci.* **2021**, *8*, 2101295.
[4] Z. Cao, F. Hu, C. Zhang, S. N. Zhu, M. Xiao, X. Wang, *Adv. Photonics* **2020**, *2*, 054001.
[5] S. Tadepalli, J. M. Slocik, M. K. Gupta, R. R. Naik, S. Singamaneni, *Chem. Rev.* **2017**, *117*, 12705.
[6] G. Isapour, M. Lattuada, *Adv. Mater.* **2018**, *30*, 1707069.
[7] Y. Wang, H. Cui, Q. Zhao, X. Du, *Matter* **2019**, *1*, 626.
[8] K. Chen, J. He, D. Zhang, L. You, X. Li, H. Wang, J. Mei, *Nano Lett.* **2021**, *21*, 4500.
[9] H. S. Kang, S. W. Han, C. Park, S. W. Lee, H. Eoh, J. Baek, D.-G. Shin, T. H. Park, J. Huh, H. Lee, *Sci. Adv.* **2020**, *6*, eabb5769.
[10] T. Yamakado, S. Saito, *J. Am. Chem. Soc.* **2022**, *144*, 2804.
[11] Y. Zhang, B. Dong, A. Chen, X. Liu, L. Shi, J. Zi, *Adv. Mater.* **2015**, *27*, 4719.
[12] Y. Yang, X. Zhang, Y. Chen, X. Yang, J. Ma, J. Wang, L. Wang, W. Feng, *ACS Appl. Mater. Interfaces* **2021**, *13*, 41102.
[13] J. Ma, Y. Yang, C. Valenzuela, X. Zhang, L. Wang, W. Feng, *Angew. Chem., Int. Ed.* **2022**, *61*, e202116219.
[14] F. Fu, L. Shang, Z. Chen, Y. Yu, Y. Zhao, *Sci. Rob.* **2018**, *3*, eaar8580.
[15] H. Liu, S. Wei, H. Qiu, M. Si, G. Lin, Z. Lei, W. Lu, L. Zhou, T. Chen, *Adv. Funct. Mater.* **2021**, *32*, 2108830.

[16] D. Kim, K.-S. Hwang, J.-H. Kim, C. Lee, J.-Y. Lee, *ACS Appl. Polym. Mater.* **2021**, *3*, 2902.
[17] F. Meng, B. Ju, Z. Wang, R. Han, Y. Zhang, S. Zhang, P. Wu, B. Tang, *J. Am. Chem. Soc.* **2022**, *144*, 7610.
[18] X. Fei, T. Lu, J. Ma, W. Wang, S. Zhu, D. Zhang, *ACS Appl. Mater. Interfaces* **2016**, *8*, 27091.
[19] S. Yu, Z. Han, X. Jiao, D. Chen, C. Li, *RSC Adv.* **2016**, *6*, 66191.
[20] T. Y. Huang, H. W. Huang, D. D. Jin, Q. Y. Chen, J. Y. Huang, L. Zhang, H. L. Duan, *Sci. Adv.* **2020**, *6*, eaav8219.
[21] Y. Hu, H. Yuan, S. Liu, J. Ni, Z. Lao, C. Xin, D. Pan, Y. Zhang, W. Zhu, J. Li, D. Wu, J. Chu, *Adv. Mater.* **2020**, *32*, 2002356.
[22] R. Li, D. Jin, D. Pan, S. Ji, C. Xin, G. Liu, S. Fan, H. Wu, J. Li, Y. Hu, D. Wu, L. Zhang, J. Chu, *ACS Nano* **2020**, *14*, 5233.
[23] C. Xin, D. Jin, Y. Hu, L. Yang, R. Li, L. Wang, Z. Ren, D. Wang, S. Ji, K. Hu, D. Pan, H. Wu, W. Zhu, Z. Shen, Y. Wang, J. Li, L. Zhang, D. Wu, J. Chu, *ACS Nano* **2021**, *15*, 18048.
[24] M. Malinauskas, A. Žukauskas, S. Hasegawa, Y. Hayasaki, V. Mizeikis, R. Buividas, S. Juodkazis, *Light: Sci. Appl.* **2016**, *5*, e16133.
[25] Y. Hu, Z. Wang, D. Jin, C. Zhang, R. Sun, Z. Li, K. Hu, J. Ni, Z. Cai, D. Pan, *Adv. Funct. Mater.* **2020**, *30*, 1907377.
[26] S. Kawata, H. B. Sun, T. Tanaka, K. Takada, *Nature* **2001**, *412*, 697.
[27] L. Yang, F. Mayer, U. H. Bunz, E. Blasco, M. Wegener, *Light: Adv. Manuf.* **2021**, *2*, 296.
[28] M. Del Pozo, C. Delaney, C. W. M. Bastiaansen, D. Diamond, A. Schenning, L. Florea, *ACS Nano* **2020**, *14*, 9832.
[29] W. Zhang, H. Wang, H. Wang, J. Y. E. Chan, H. Liu, B. Zhang, Y. F. Zhang, K. Agarwal, X. Yang, A. S. Ranganath, H. Y. Low, Q. Ge, J. K. W. Yang, *Nat. Commun.* **2021**, *12*, 112.
[30] H. Kim, J. Ge, J. Kim, S.-e. Choi, H. Lee, H. Lee, W. Park, Y. Yin, S. Kwon, *Nat. Photonics* **2009**, *3*, 534.
[31] D. Jin, Q. Chen, T.-Y. Huang, J. Huang, L. Zhang, H. Duan, *Mater. Today* **2020**, *32*, 19.
[32] M. P. Stocker, L. Li, R. R. Gattass, J. T. Fourkas, *Nat. Chem.* **2011**, *3*, 223.
[33] V. Hahn, T. Messer, N. M. Bojanowski, E. R. Curticean, I. Wacker, R. R. Schröder, E. Blasco, M. Wegener, *Nat. Photonics* **2021**, *15*, 932.
[34] W. Zhang, H. Wang, H. Wang, J. Y. E. Chan, Q. Ruan, H. Liu, J. K. Yang, *Mater. Today Proc.* **2022**, https://doi.org/10.1016/j.matpr.2022.09.242.
[35] F. Wang, M. Liu, C. Liu, Q. Zhao, T. Wang, Z. Wang, X. Du, *Sci. Adv.* **2022**, *8*, eabp9369.
[36] Y. Liu, H. Wang, J. Ho, R. C. Ng, R. J. H. Ng, V. H. Hall-Chen, E. H. H. Koay, Z. Dong, H. Liu, C. W. Qiu, J. R. Greer, J. K. W. Yang, *Nat. Commun.* **2019**, *10*, 4340.
[37] M. Schmid, D. Ludescher, H. Giessen, *Opt. Mater. Express* **2019**, *9*, 4564.
[38] Y. W. Lee, H. Ceylan, I. C. Yasa, U. Kilic, M. Sitti, *ACS Appl. Mater. Interfaces* **2021**, *13*, 12759.